buildings

MDPI

Article

Experimental Study on Seismic Performance of Partially Corroded Squat RC Shear Walls in Coastal Environment

Yuanyuan Song [1], Jian Wang [2,*] and Jinsheng Du [1]

[1] School of Civil Engineering, Beijing Jiaotong University, Beijing 100044, China; jshdu@bjtu.edu.cn (J.D.)
[2] School of Civil Engineering, Sun Yat-sen University, Guangzhou 510275, China
* Correspondence: wangj833@mail.sysu.edu.cn

Abstract: In coastal environments, squat reinforced concrete (RC) shear walls are susceptible to local accumulation of moisture and chloride salts, causing local corrosion in the shear walls, which in turn affects their seismic performance. Four squat RC shear wall specimens were designed considering the corrosion locations and the heights of the corroded area. The seismic performance of partially corroded squat RC shear wall specimens was analyzed through a quasi-static test. The results show that as the height of the corroded area increases from 15% to 25% of the total height, the area of the hysteresis loop of the shear walls obviously decreases. As the height of the corroded area increases from 0 to 15% and 25% of the total height, the peak and ultimate displacements of shear walls are, respectively, reduced by 6.7% and 19.2% in the positive loading direction, and are, respectively, reduced by 22.3% and 18.3% in the negative loading direction. Compared with the unilateral corroded shear wall, the area of the hysteresis loop and the stiffness of the bilateral corroded shear wall remain approximately unchanged, and the peak and ultimate displacements, the shear strain, and the ratio of shear deformation to horizontal displacement are reduced. Compared with the uncorroded shear wall, the hysteresis loop of the unilateral corroded shear wall is plump, the displacement ductility ratio and the plastic rotation angle are both increased, and the stiffness degradation is relatively slow.

Keywords: squat RC shear wall; partial corrosion; quasi-static test; seismic performance

Citation: Song, Y.; Wang, J.; Du, J. Experimental Study on Seismic Performance of Partially Corroded Squat RC Shear Walls in Coastal Environment. *Buildings* **2024**, *14*, 404. https://doi.org/10.3390/buildings14020404

Academic Editor: Jun-Mo Yang

Received: 20 December 2023
Revised: 24 January 2024
Accepted: 29 January 2024
Published: 2 February 2024

1. Introduction

Reinforced concrete (RC) shear walls can withstand the self-weight and horizontal loads of a building, which can also effectively control the lateral displacement of the building [1,2]. RC shear walls are commonly used as lateral force-resisting structural systems in high-rise buildings and nuclear power plants, and they are often used as the first line of defense for seismic resistance of building structures. According to the aspect ratio (height to width), RC shear walls can be divided into slender walls, medium-slender walls, and squat walls. Squat walls with aspect ratios less than approximately 1.0 to 1.5 generally exhibit shear dominant responses, slender walls with aspect ratios greater than 2.5 to 3.0 demonstrate flexure-controlled responses, and medium-slender walls (between 1.5 and 2.5) usually behave in the coupled flexural and shear response [3,4]. Under vertical forces and in-plane horizontal forces, the mechanical properties and damage patterns of slender, medium-slender, and squat walls are different [5]. During urban construction and building renovation, squat RC shear walls are widely used in building structures with transfer floors with large bottom spaces [6,7].

Corrosion of steel bars is one of the main factors that reduces the durability of RC structures in coastal or marine environments [8–11]. The relative humidity and chloride ion concentration in coastal areas are higher, so the corrosion rate of steel bars in RC structures is higher than that in inland areas [12]. Corrosion can reduce the cross-sectional area of steel bars and degrades their mechanical properties [13,14]. Moreover, the volume expansion of the corrosion products causes cracks in concrete cover along the axial direction of the steel bars and weakens the bonding performance between the steel bars and the surrounding concrete [15–17]. In addition, a large number of RC structures in the coastal environment are located in the seismic zones, which are affected by strong earthquakes during their service. Therefore, it is of great theoretical value and practical engineering significance to study the effect of steel corrosion on the seismic performance of RC structures. At present, many scholars have studied the seismic performance of corroded RC structures, and a large number of valuable results have been obtained [3,12,16,18–23].

Up to now, the seismic performance of RC shear walls before and after corrosion has been investigated by many researchers [3,20–29]. In the aspect of research on seismic performance of corroded RC shear walls, Oyamoto et al. [20] studied the effect of steel corrosion rate on the shear strength of RC shear walls through the in-plane shear test. Zhou et al. [3] conducted a salt spray accelerated corrosion test and quasi-static test on seven RC shear walls and found that chloride ion erosion would deteriorate the mechanical properties of the materials, and that it ultimately reduced the seismic performance of RC shear walls. Zheng et al. [21] carried out quasi-static tests on squat RC shear walls with different degrees of corrosion, and studied the failure mode, bearing capacity, deformation performance, energy dissipation capacity, and shear deformation performance of shear walls. Li et al. [22] investigated the effect of different steel corrosion rates on the seismic performance of RC shear walls by conducting accelerated corrosion test and quasi-static test on four RC shear wall specimens. Yang et al. [23] conducted an accelerated corrosion test and quasi-static test on six T-shaped RC shear wall specimens, and found that the bearing capacity, deformation capacity, stiffness, cumulative energy dissipation capacity, and the ratio of shear deformation to total deformation of the specimens all showed a decreasing trend with the increase in the corrosion degree of the steel bars. However, the above related studies all carried out overall corrosion of RC shear walls to study their seismic performance. As is well known, the side of the shear walls facing the external environment of the building structure in the coastal environments is directly eroded by the chloride ions. On the one hand, chloride ions often accumulate in the roots of buildings with precipitation and evaporation. On the other hand, due to construction quality or stress problems, RC shear walls have local defects or cracking phenomena. These problems will lead to the phenomenon of local corrosion of RC shear walls. With the increase in the service life of shear walls, long-term local corrosion will cause concrete cracking and even concrete cover spalling, resulting in the degradation of the mechanical properties of steel bars, which will seriously affect the mechanical properties and seismic performance of shear walls. The effects of global corrosion and local corrosion on the seismic performance of shear walls are different, and the existing studies cannot provide practical guidance for locally corroded squat shear walls. At present, the seismic performance of partially corroded squat RC shear walls is still unknown and needs to be explored.

To fill this research gap, four squat RC shear wall specimens were designed and fabricated considering the corrosion locations and the heights of the corroded area. Firstly, the local corrosion of the shear walls was realized by an accelerated corrosion test. Subsequently, the quasi-static test of the corroded shear walls was carried out. Finally, the failure process, hysteretic curve, bearing capacity, deformation performance, and stiffness degradation of the corroded shear walls were analyzed, and the seismic performance of the partially corroded squat RC shear walls was revealed. The flowchart is shown in Figure 1.

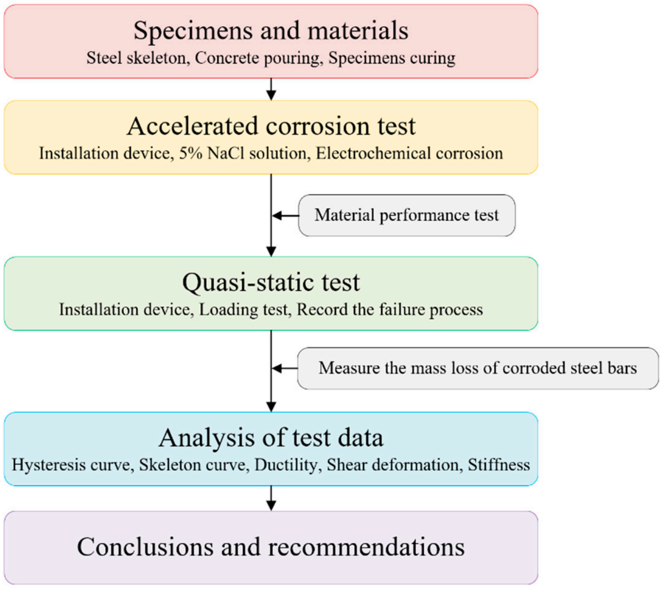

Figure 1. Research flowchart.

2. Experimental Program

2.1. Design of Specimens

To study the seismic performance of partially corroded squat RC shear walls, four squat RC shear wall specimens were designed according to the Chinese Standard GB 50010 [30]. The aspect ratio of the specimens was 1.0. The width, height, and thickness of the wall were 600, 600, and 100 mm, respectively, and the thickness of concrete cover was 10 mm, as depicted in Figure 2. Concrete with a strength grade of C40 adopted P.O 42.5R cement as cementitious material, the particle size of coarse aggregate was 5–20 mm, the natural river sand was selected as fine aggregate, and the mixing water was tap water. The detailed mix proportion of concrete is listed in Table 1. The 28-day cubic compressive strength of the concrete was 49.65 MPa, and the type of steel bars was HRB400. The diameter and spacing of the steel bars distributed inside the wall were 6 and 150 mm, respectively. In the body of wall specimens, the reinforcement ratio of longitudinal and horizontal distributions of steel bars was 0.42% and 0.38%, respectively. The diameter and the reinforcement ratio of the longitudinal reinforcement of the hidden columns were 12 mm and 4.52%, respectively. The diameter, spacing, and the reinforcement ratio of the stirrups of the hidden columns were 6 mm, 150 mm, and 0.38%, respectively. Specific dimensions and reinforcement of the specimens are shown in Figure 2. The physical picture is shown in Figure 3.

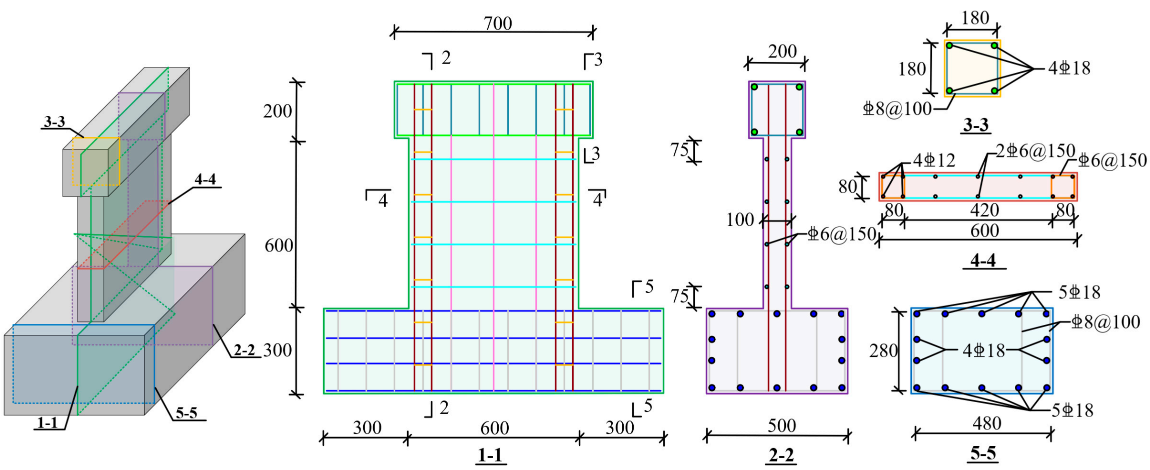

Figure 2. Dimensions and reinforcement (unit: mm).

Table 1. Mix proportion of concrete (unit: kg/m^3).

Cement	Water	Sand	Gravel	Water Reducer	Fly Ash	Slag
249	163	736	1059	8.3	79	87

Figure 3. Shear wall specimens after curing.

2.2. Accelerated Corrosion Test

The different corrosion conditions of shear wall specimens are shown in Figure 4 and Table 2. A water tank containing 5% NaCl solution by mass fraction was pre-set in the target corroded position of specimens, as shown in Figure 5.

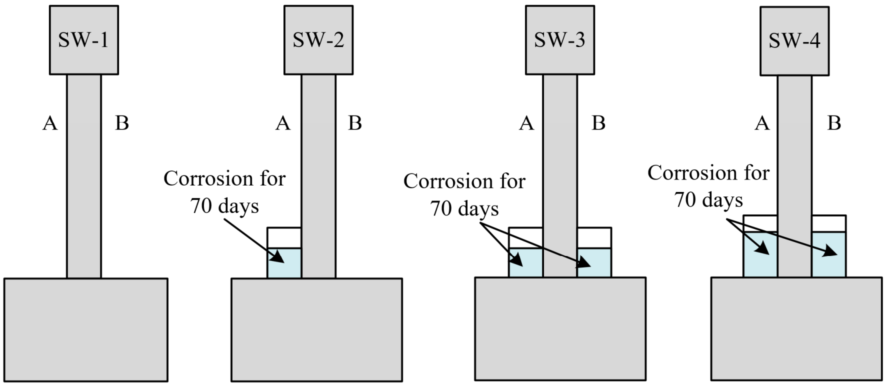

(**a**)

(**b**)

Figure 4. Shear wall specimens with different corrosion conditions. (**a**) Schematic drawing; (**b**) physical picture.

Table 2. Different corrosion conditions.

Specimen Label	Corrosion Time of Side A	Corrosion Height/Total Height of Side A	Corrosion Time of Side B	Corrosion Height/Total Height of Side B
SW-1	0	0	0	0
SW-2	70 days	15%	0	0
SW-3	70 days	15%	70 days	15%
SW-4	70 days	25%	70 days	25%

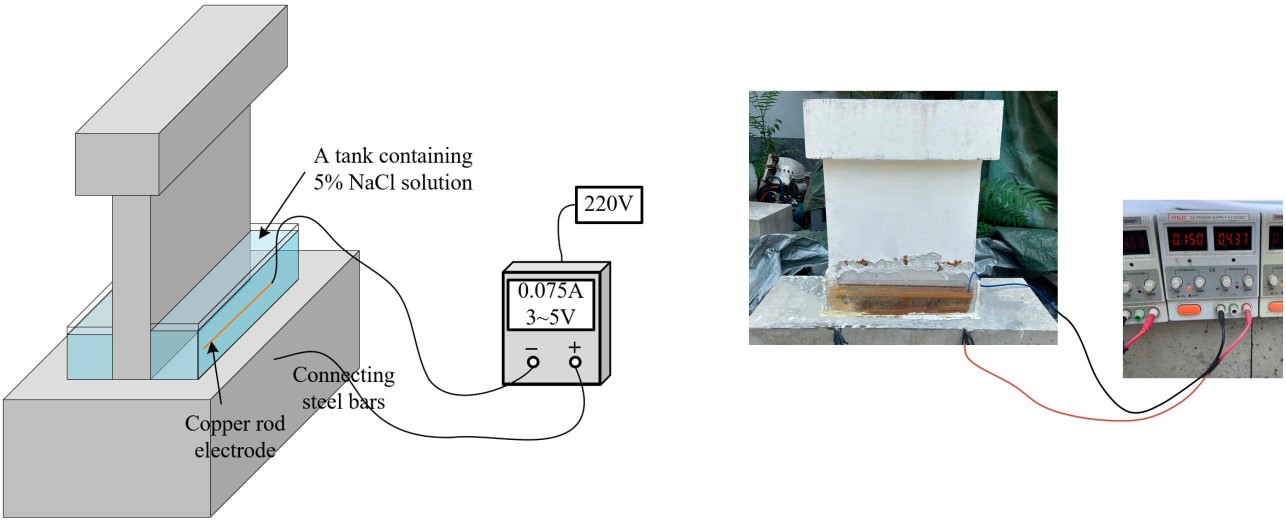

(**a**) (**b**)

Figure 5. Schematic diagram of electrochemical corrosion. (**a**) Schematic drawing; (**b**) physical picture.

In the laboratory, the constant current method is often adopted to accelerate the corrosion of RC members [31–34], which can achieve steel corrosion in a short time, but it is difficult to achieve the same corrosion characteristics with steel corrosion in the natural environment. Some scholars [35–37] found that when the current density was lower than 200 $\mu A/cm^2$ during the accelerated corrosion process, the corrosion characteristics of steel bars were close to those of the steel bars in RC structures in natural environment. Therefore, the current density of this corrosion test was set to 180 $\mu A/cm^2$.

Before the accelerated corrosion test, the squat RC shear wall specimens were immersed in 5% NaCl solution for 72 h, so as to ensure full contact between the electrolyte solution and the concrete, and a closed circuit was formed with the steel bars, as shown in Figure 5. During the process of accelerate corrosion, a copper rod in the water tank was connected to the negative terminal of a DC power supply with an output voltage of 0–30 V and an output current of 0–5 A, and the steel bars within 90 mm (SW-2 and SW-3) or 150 mm (SW-4) height of the wall were connected to the positive terminal of the DC power supply. During the accelerated corrosion test, the corrosion-induced cracking of the specimens was recorded.

2.3. Quasi-Static Test

In the structural laboratory, the quasi-static test was carried out on the RC shear wall specimens after the accelerated corrosion test. During loading, YHD-100 displacement meters with a measuring range of 50 mm were set on the top beam, bottom beam, and diagonals of the A and B sides to evaluate the deformation capacity of the specimens. The loading device and displacement meters arrangement are illustrated in Figure 6.

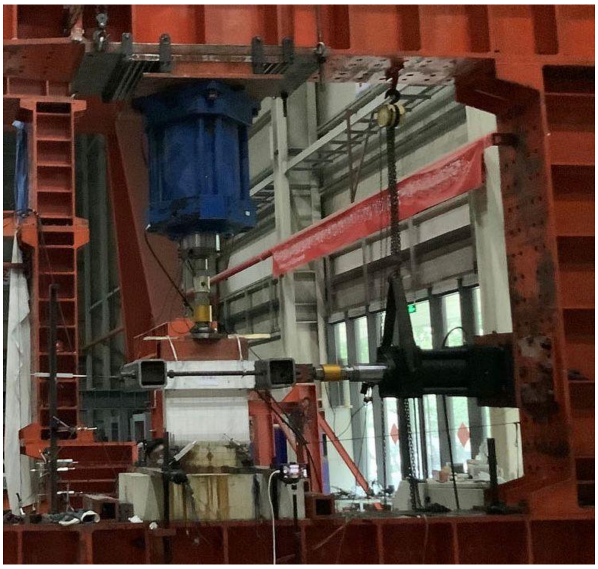

(**a**)

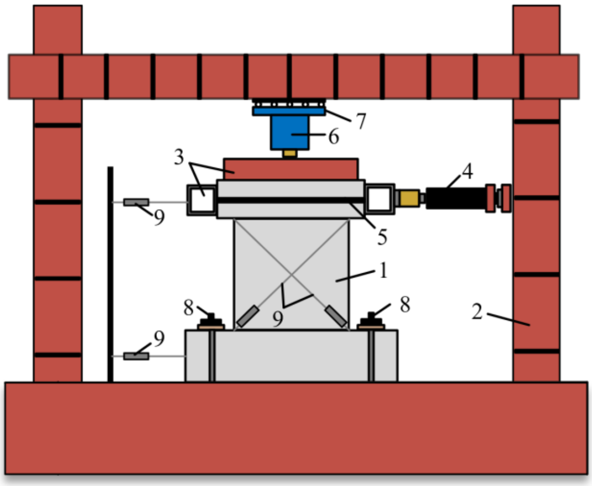

(**b**)

Figure 6. Testing setup. (**a**) General view; (**b**) schematic layout.

Firstly, a vertical load was applied to the specimen to reach the axial compression ratio of 0.1, which remained constant during the test process. Then, a reciprocating horizontal load was applied to the specimen in the form of displacement by a hydraulic actuator. With a displacement increment of a 0.2% displacement angle, the horizontal displacement increment was 1.4 mm. In the early cycles, in order to better determine the cracking displacement, the displacement angle increments of 0.05% and 0.1% were adopted, that is, the horizontal displacement increments were 0.35 and 0.7 mm, respectively, as shown in Figure 7. Relevant studies [38,39] showed that the failure mode of squat RC shear walls was brittle failure without a clear yield point. According to the Chinese Standard JGJ/T101 [40], the displacement-controlled amplitude loading method was adopted in this test, and each displacement amplitude was cyclically loaded three times. The loading test stopped when the horizontal load applied to the specimens dropped to 85% of the peak load or the specimens were obviously damaged.

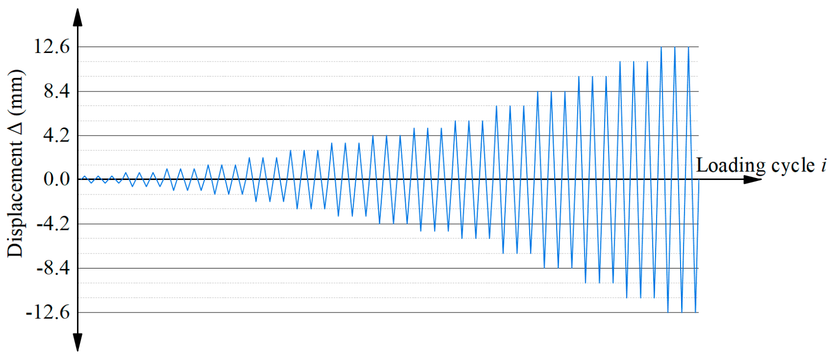

Figure 7. Loading history.

2.4. Measurement of Mass Loss of Steel Bars

After the quasi-static test, the concrete was crushed to remove the steel bars in specimens, and the mass loss of the steel bars was measured. According to the Chinese Standard GB/T 50082 [41], after the steel bars were removed from the specimens, the concrete attached to the steel bars was scraped, and then the corroded steel bars were pickled with 12% hydrochloric acid solution. After being rinsed with clean water, the steel bars were neutralized with lime water, and then rinsed with clean water and dried for 4 h. Finally, each corroded steel bar was weighed, as shown in Figure 8. The average mass loss of steel bars in the corroded area of the specimens was calculated according to the following Equation (1):

$$L_{\mathrm{m}} = \frac{m_0 - m}{m_0} \times 100 \tag{1}$$

where L_{m} is the mass loss of a steel bar, %; and m_0 and m are the masses of a steel bar before and after corrosion, respectively, g.

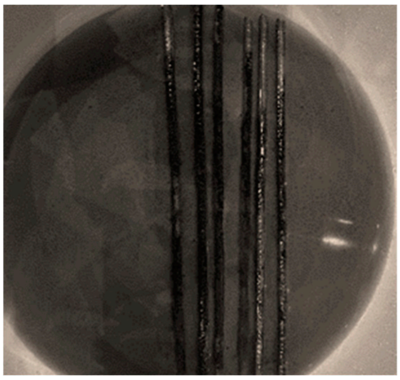

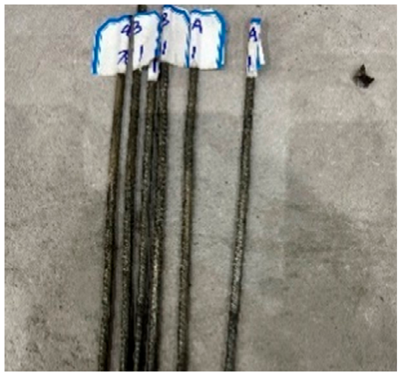

(**a**) (**b**)

Figure 8. Steel bars after corrosion. (**a**) Hydrochloric acid pickling; (**b**) after drying.

3. Results and Discussion

3.1. Analysis of Mass Loss of Steel Bars

The average mass loss of the steel bars in the corroded area of the specimens is tabulated in Table 3. When comparing SW-3 with SW-4, the change in the height of the corroded area has little effect on the average mass loss of steel bars. This is because the main difference between the corrosion of SW-3 and SW-4 is the total length of the corroded steel bars. For SW-2 and SW-3, under the same corrosion days, the average mass loss of the specimens with unilateral corrosion is smaller than that of the specimens with bilateral corrosion, indicating that bilateral corrosion is not a simple superposition of unilateral corrosion. The steel bars in SW-2B away from the water tank are not completely uncorroded, and rust products have also appeared in some local areas in this side; compared to the uncorroded steel bars in SW-2B, the amount of corroded steel bars is very small, and calculating the average mass loss of these steel bars is meaningless. During the corrosion test, SW-2B also has current passing through, hence, the current passing through the steel bars in SW-2A is smaller than the planned value, so SW-2 corrodes less than SW-3.

Table 3. Average mass loss of steel bars in the corroded area.

Specimen Label	Corroded Side	Corrosion Days/Days	Target Corrosion Height/mm	Average Mass Loss/%
SW-1	—	0	0	0
SW-2	A	70	90	13.05
	B	0	0	0
SW-3	A and B	70	90	16.22
SW-4	A and B	70	150	16.64

3.2. Failure Process of Specimens

The failure modes of the four shear wall specimens are shown in Figure 9. The failure process of the specimens is as follows.

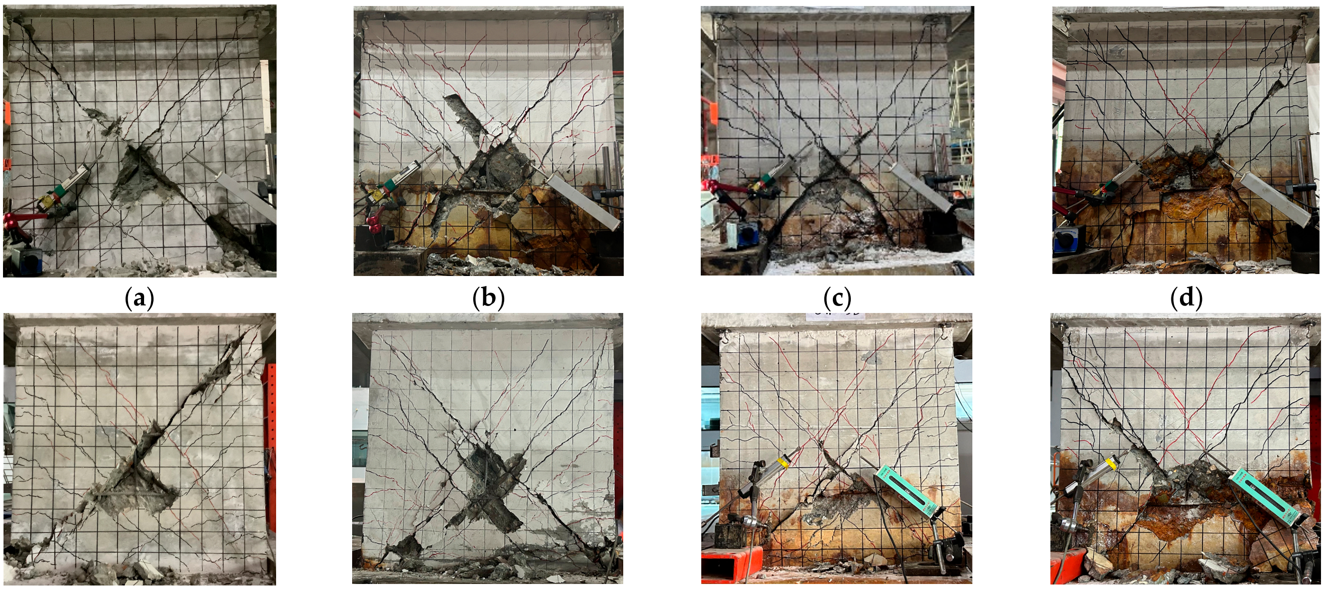

Figure 9. Failure mode of the specimens. (**a**) SW-1A; (**b**) SW-2A; (**c**) SW-3A; (**d**) SW-4A; (**e**) SW-1B; (**f**) SW-2B; (**g**) SW-3B; (**h**) SW-4B.

(1) SW-1

In the positive loading direction, the first oblique crack appears on both the A and B sides of the specimen when the displacement reaches 2.1 mm. As the displacement reaches 2.8 mm, the second and third oblique cracks appear on the A side of the specimen, and the second, third, and fourth oblique cracks appear on the B side, and some small cracks appear on the A and B sides and the lateral tensile surface. As the displacement reaches 7.7 mm, the concrete near the main oblique crack begins to spall. The concrete on the A and B sides slightly peels off at the crack of the compression root. The width of the main oblique crack reaches about 4 mm when the displacement is 9.1 mm. As the displacement reaches 11.2 mm, the concrete at the middle intersection of the oblique cracks on the A and B sides peels off and some steel bars are exposed. The horizontal load has dropped to 85% of the peak load, which is considered to be the failure of the specimen.

In the negative loading direction, when the displacement reaches 2.1 mm, three parallel oblique cracks appear on the A side of the specimen and four parallel oblique cracks appear on the B side at the same time. When the displacement is 2.8 mm, the cracks further extend and widen, almost diagonally distributed, and several small cracks appear on both the A and B sides and the lateral tensile surface. As the displacement reaches 8.4 mm, the concrete at the root of the sides is severely damaged and is about to fall off in a large area. When the displacement reaches 9.1 mm, the concrete near the main oblique crack begins to spall, and the spalling at the compression root cracks is serious. When the displacement is 11.2 mm, the concrete at the middle intersection of the oblique cracks on the A and B sides peels off and some steel bars are exposed. The horizontal load has dropped to 85% of the peak load, which is considered to be the failure of the specimen.

(2) SW-2

In the positive loading direction, the first oblique crack appears on both the A and B sides of the specimen when the displacement is 0.7 mm. When the displacement reaches 1.05 mm, the side surface of the specimen is under tension, and several horizontal cracks appear at the root and top. The oblique crack continues to extend, and a second crack appears at the position parallel to the first crack on the B side. As the displacement reaches 2.1 mm, there are five tensile cracks on the lateral tensile surface of the specimen, and all of them have been completely penetrated. The concrete on A and B sides appears to be slightly spalling at the cracks of the compression root when the displacement reaches 5.6 mm. When the displacement reaches 9.8 mm, the concrete at the root of the specimen begins to spall in a large area, and the phenomenon of concrete spalling also occurs at the oblique cracks in the middle of the specimen. As the displacement reaches 12.6 mm, the concrete in the middle of the A side peels off extensively, while the B side peels off slightly. The horizontal load drops to 85% of the peak load, indicating that the specimen is a failure.

In the negative loading direction, the first crack appears on both the A and B sides of the specimen when the displacement reaches 1.4 mm. When the displacement is 2.8 mm, a second crack appears simultaneously on the A and B sides of the specimen and is parallel to the location of the first crack. With the increase in displacement, the small oblique cracks increase, and a few of them are connected with corrosion-induced cracks. When the displacement reaches 5.6 mm, concrete spalling occurs on the B side. When the displacement is 9.8 mm, the concrete at the root of the specimen is slightly spalling. With the increase in displacement, the concrete spalling becomes more and more serious. When the displacement is 12.6 mm, the concrete on both the A and B sides peels off extensively, and the horizontal load has dropped to 85% of the peak load, indicating that the specimen has failed.

(3) SW-3

In the positive loading direction, the first oblique crack appears on both the A and B sides of the specimen when the displacement reaches 1.05 mm. As the displacement reaches 1.4 mm, the second oblique crack appears on the A and B sides of the specimen, and it is parallel to the first one. There are several horizontal through cracks on the lateral tensile surface. As the displacement reaches 2.1 mm, a horizontal wide crack connecting the corrosion-induced cracks and a vertical crack distributed along the steel bars of the hidden columns appear in the corroded area on B side. When the displacement reaches 7.0 mm, the concrete in the corroded area on the B side begins to fall off. When the displacement reaches 9.8 mm, a large area of concrete peeling occurs at the intersection of the oblique cracks on the A and B sides. When the horizontal load drops to 85% of the peak load, it is considered that the specimen has failed.

In the negative loading direction, when the displacement reaches 1.4 mm, the first oblique crack appears on both the A and B sides of the specimen. When the displacement is 2.1 mm, the second oblique crack appears on the A and B sides of the specimen, and it is parallel to the first one. There are several horizontal through cracks on the lateral tensile surface. The combined action of corrosion and load causes a large piece of concrete cover at the bottom of the A side to peel off. As the displacement reaches 3.5 mm, the small oblique cracks of the specimen increase continuously, and there are two cracks through the lateral tensile surface. Small oblique cracks extend and widen, and the number of horizontal penetrating cracks on the lateral tensile surface gradually increases. When the displacement reaches 9.8 mm, the concrete at the middle intersection of the oblique cracks on the A and B sides and peels off in a large area. The horizontal load has dropped to 85% of the peak load, which is considered to be the failure of the specimen.

(4) SW-4

In the positive loading direction, the first oblique crack appears on the B side of the specimen when the displacement reaches 1.4 mm. When the displacement is 2.8 mm, the second oblique crack on the B side of the specimen appears simultaneously with the first and second cracks on the A side. But there is no obvious crack on the lateral tensile surface. When the displacement reaches 4.9 mm, the concrete in the corroded area on the A side begins to fall off, the horizontal cracks on the lateral tensile surface increase, and one of them runs through. When the displacement reaches 8.4 mm, a large area of concrete peeling occurs at the intersection of oblique cracks on A and B sides. When the horizontal load has dropped to 85% of the peak load, it is considered that the specimen has failed.

In the negative loading direction, as the displacement reaches 1.4 mm, the first oblique crack appears on both A and B sides of the specimen, but the crack width is extremely small, and the length is short. As the displacement reaches 2.8 mm, the oblique cracks on the A and B sides of the specimen expand and connect with the corrosion-induced cracks in the corroded area, and two horizontal cracks are connected on the lateral tensile surface. The oblique cracks are increasing, extending, and widening, the horizontal through cracks on the lateral tensile surface are increasing gradually, and the cracks in the corroded part are obviously wider. As the displacement reaches 7.0 mm, the concrete falls off in a large area, and the width of oblique cracks on the A and B sides reaches 2 mm. The horizontal load has dropped to 85% of the peak load, which is considered to be the failure of the specimen.

By comparing SW-1, SW-3, and SW-4, it can be found that with the increase in the height of the corroded area, the horizontal displacement corresponding to the failure of the specimen decreases. When comparing SW-2 with SW-3, it can be seen that the horizontal displacement corresponding to the failure of bilateral corroded specimens is smaller than that of unilateral corroded specimens. However, compared with SW-1, the horizontal displacement corresponding to the failure of SW-2 increases. It is also found that the quantity of oblique cracks on the specimens with larger degrees of corrosion is small, while there are many oblique cracks and horizontal cracks on the uncorroded specimen. The reason is that after the steel bars are corroded, the adhesion with the concrete is reduced, and the effective anchoring length of steel bars is increased, while the spacing of cracks is proportional to the effective anchoring length of steel bars, so the number of cracks is reduced. In addition, the cracks of the uncorroded specimen mostly appear below the main oblique cracks. With the increase in the corrosion range and the height of the corroded area, the cracks above the main oblique cracks gradually increase, showing an oblique network on the specimens. The main reason is that the corrosion expansion of the steel bars leads to the extrusion cracking of concrete, increasing the defects in concrete; after the horizontal load is applied, the internal defects of concrete gradually develop into external cracks, and as a result, obvious wider cracks, above which the main oblique cracks appear in the position with relatively small stress.

During the loading period, cracks appear continuously and extend along the 45° direction, and the specimens are divided into oblique meshes. In the failure stage, with a sharp decrease in horizontal load, the diagonal cracks of the specimens are widened, and the concrete in the central area of the specimens is broken and peels off. All four specimens show obvious shear brittle failure. Zhou et al. [3] conducted quasi-static test on corroded shear walls with different aspect ratios, and they found that the shear wall was experiencing shear brittle failure when the aspect ratio was 1.0, which was basically consistent with the results of this paper.

3.3. Hysteretic Curve

The hysteretic curve reflects the relationship between the force and deformation of structures under low-cycle reciprocating loads. The area of the hysteresis loop surrounded by each push and pull cycle of the load represents the energy dissipation capacity of structures, which is the analysis basis of the seismic elastic–plastic response of structures. The hysteretic curves of the four specimens are obtained by a quasi-static test, as shown in Figure 10.

Figure 10 shows that the hysteretic curves of specimens have some common characteristics. The hysteretic curve of the specimens before cracking shows a basic linear reciprocating change, with small stiffness changes, and the loading and unloading curves basically overlap. After reaching the yield point, the loading and unloading stiffness of the specimens begin to decrease, and the residual deformation increases after unloading. With the increase in loading displacement and the accumulation of damage, the area of the hysteresis loop increases, and the energy dissipation capacity is improved. In the process of three cyclic loadings under the same displacement amplitude, the stiffness degradation of the specimens is obvious during the second and third cyclic loading, and the nonlinear characteristics of the specimens are obvious. After reaching the peak load, the hysteretic curve enters a transition zone, and with the increase in displacement, the bearing capacity of the specimens does not decrease significantly, showing a certain deformation capacity. With the accumulation of damage over time, the bearing capacity of the specimens begins to decrease significantly, and there is obvious residual deformation, which increases with the displacement multiples and the number of cycles.

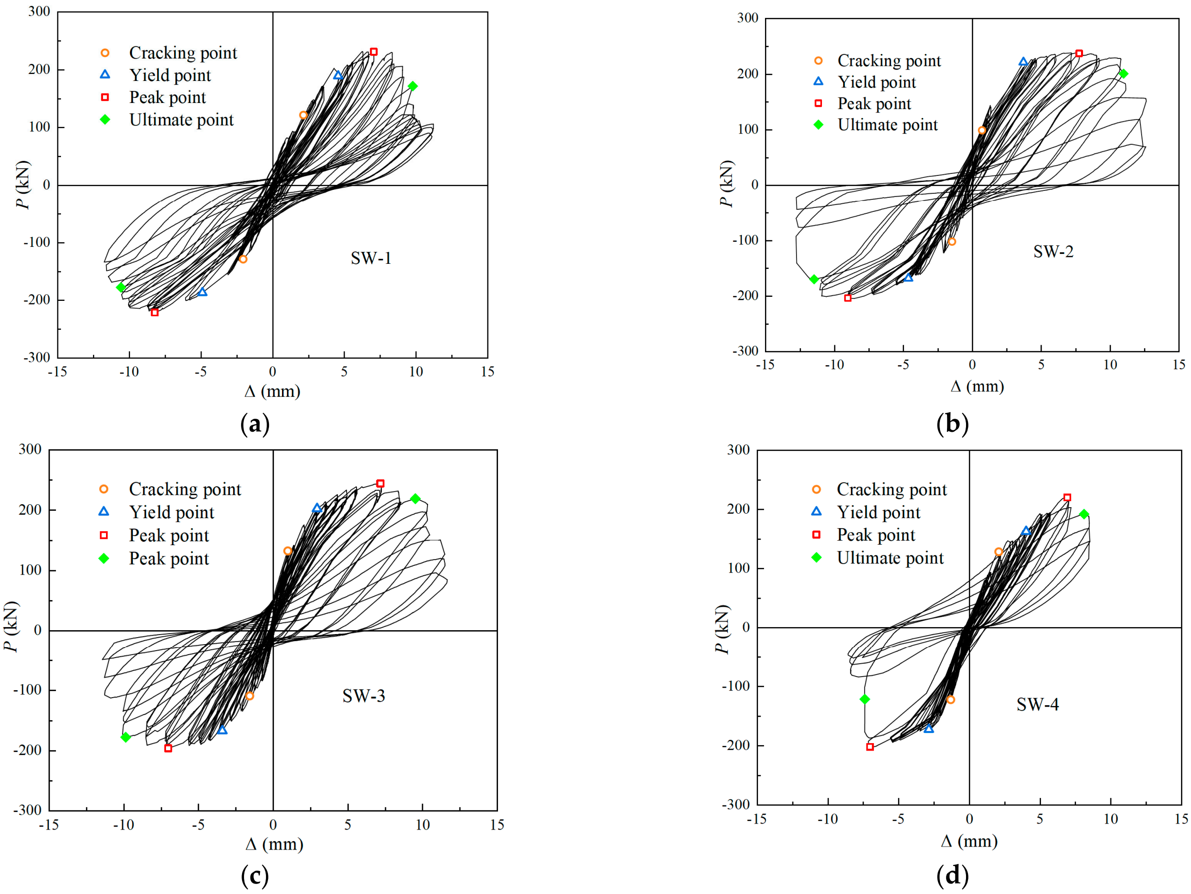

Figure 10. Hysteretic curves. (**a**) SW-1; (**b**) SW-2; (**c**) SW-3; (**d**) SW-4.

Compared with the uncorroded SW-1, the hysteresis loop of the SW-2 is plump and the area is larger, indicating that the energy dissipation capacity of SW-2 has been improved. The reasons may be as follows: (1) the corrosion of the steel bars will cause changes in the bonding performance between steel bars and concrete. When the corrosion rate of the steel bars is low, the appearance of a small amount of corrosion products can improve the bonding performance of steel bars and concrete, thereby improving the energy dissipation capacity of structures. (2) The number of specimens is relatively small, and the obtained test results may have discreteness. When comparing SW-3 with SW-4, the elevation of the corrosion area height distinctly diminishes the area of the hysteresis loop. Particularly noteworthy is the case of SW-4, where a sudden alteration in the hysteresis loop area is observed in the negative loading direction once the horizontal displacement exceeds 7 mm, resulting in a rapid decline in bearing capacity. The initial negative hysteresis curve of SW-4 manifests a minute area, nearly approaching zero, underscoring the substantial influence of corrosion area height on energy dissipation. Furthermore, when comparing the hysteresis curves of SW-2 with unilateral corrosion to those of SW-3 with bilateral corrosion, it becomes evident that, at the same height of corrosion area, their differences are minimal, and the hysteresis curves exhibit similar areas and pinching trends, showcasing a comparable energy dissipation capacity between the two.

3.4. Skeleton Curve

By connecting the peak values of hysteresis loops as shown in Figure 10, a skeleton curve of each specimen can be obtained, as depicted in Figure 11. The skeleton curve can reflect the mechanical properties, such as bearing capacity, stiffness, ductility, and deformation of the specimens at different stages. The loads and displacements corresponding to the cracking points, yield points, peak points, and ultimate points of the skeleton curves are given in Table 4, where the yield points are determined by the equivalent energy method [42]. The equivalent energy method adopts the method of the equal area surrounded by the *P*-Δ skeleton curve to determine the equivalent yield point, as shown in Figure 12. The A point and B point are obtained by equalizing the area of A_1 and A_2. The vertical line passing through point A intersects with the *P*-Δ skeleton curve at point C, and the point C is the equivalent yield point. The corresponding load and displacement of the equivalent yield point are the yield load and yield displacement, respectively. Due to the brittle failure of squat RC shear walls, the bearing capacity declines rapidly after reaching the peak load, and the ultimate load is taken as 85% of the peak load. Some studies [43,44] found that, when conducting quasi-static test on structures, due to the Bauschinger effect, the load and displacement values on the hysteretic curves show incomplete symmetry in the positive and negative loading directions, which is also reflected in Table 4.

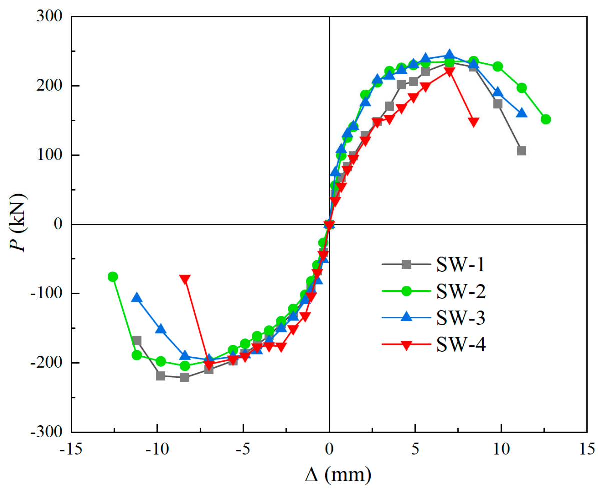

Figure 11. Skeleton curves.

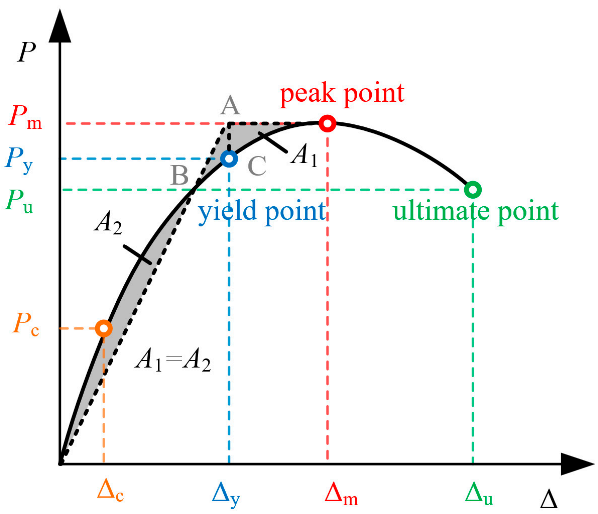

Figure 12. Definition of yield displacement and load.

Table 4. Characteristic parameters of skeleton curves.

Loading Direction	SpecimenLabel	Cracking		Yield		Peak		Ultimate		μ	θ_P/%	Initial Stiffness/ kN/mm
		P_c/kN	Δ_c/mm	P_y/kN	Δ_y/mm	P_m/kN	Δ_m/mm	P_u/kN	Δ_u/mm			
Positive	SW-1	121.82	2.10	185.67	4.51	228.8	8.34	194.48	10.22	2.27	0.82	224.56
	SW-2	99.77	0.70	194.45	3.72	238.79	7.73	202.97	11.25	3.02	1.08	161.24
	SW-3	130.88	1.05	175.15	3.02	244.3	7.21	207.66	9.09	3.01	0.87	213.99
	SW-4	132.04	2.10	157.15	4.75	220.93	6.91	187.79	7.64	1.61	0.41	136.68
Negative	SW-1	128.02	2.10	183.00	4.71	220.86	8.24	187.73	10.65	2.26	0.85	217.26
	SW-2	101.84	1.40	167.71	4.79	203.46	9.03	172.94	11.39	2.38	0.94	115.67
	SW-3	110.33	1.40	162.02	3.24	195.79	7.02	166.42	9.30	2.87	0.87	146.68
	SW-4	131.97	1.40	175.50	3.11	202.02	7.04	171.72	7.40	2.38	0.61	125.05

Table 4 shows that when comparing SW-1, SW-3, and SW-4, it can be found that as the height of the corroded area increases from 0 to 25% of the total height, the peak and ultimate displacements in the positive loading direction decrease. Compared with SW-1, the peak displacement of SW-3 and SW-4 is reduced by 13.5% and 17.1%, respectively, and the ultimate displacement is reduced by 11.1% and 25.2%, respectively. In the negative loading direction, compared with SW-1, the cracking displacement of SW-3 and SW-4 is decreased by 33.3% and 33.3%, respectively, the yield displacement is decreased by 31.2% and 34.0%, respectively, the peak displacement is decreased by 14.8% and 14.6%, respectively, and the ultimate displacement is decreased by 12.7% and 30.5%, respectively. It can be seen that with the increase in the height of the corroded area, the displacement of each characteristic point shows a downward trend as a whole. As can be seen from Table 4, compared with displacement, the influence of the height of the corroded area on the load is not obvious, which is consistent with the test results obtained by Zhou et al. [3], indicating that the influence of chloride ion erosion on the deformation capacity is greater than that on the bearing capacity, whether it is overall corrosion or local corrosion. In addition, the SW-4 with the highest height of the corroded area and the most severe corrosion has a more obvious second-order effect after yielding, and the bearing capacity decreases faster.

The curves in the elastic stage of SW-2 and SW-3 are basically coincident. Compared with SW-2, the yield, peak, and ultimate displacements of SW-3 are smaller. In the positive loading direction, the yield, peak, and ultimate displacements of SW-3 are reduced by 18.8%, 6.7%, and 19.2% compared to those of SW-2, respectively, and in the negative loading direction, the yield, peak, and ultimate displacements of SW-3 are reduced by 32.4%, 22.3%, and 18.3% compared to those of SW-2, respectively. Compared with SW-2, the yield and peak loads of SW-3 approximately show a decreasing trend.

Compared with uncorroded SW-1, the yield and peak loads of SW-2 in the positive loading direction approximately show an increasing trend, while the yield and peak loads in the negative loading direction approximately show a decreasing trend. The main reason may be that after the unilateral corrosion of SW-2, the corrosion of the steel bars in the local areas is lighter, and a small amount of corrosion products instead improve the bonding performance of steel bars and concrete. The improvement of the bonding force in the partial area during positive loading improves the bearing capacity of the shear wall to a certain extent. Due to the Bauschinger effect, the improvement in the bonding force between the steel bars and the concrete during negative loading has little effect on the bearing capacity of the shear walls, while the decrease in strength of the steel bars after corrosion plays a dominant role.

The variations in cracking load and cracking displacement of the specimens are irregular. The main reasons are as follows: (1) it is difficult to accurately judge the cracking point due to the interference of corrosion-induced cracks; (2) cracking load and cracking displacement are often only related to the strength of the concrete, and other factors, such as steel corrosion, have little effect on them.

3.5. Ductility Analysis

Ductility refers to the deformation ability of a structure or component during the period from yielding to failure (reaching the ultimate load), which is one of the important indicators to measure the structural ability in an earthquake [45]. In this paper, the ratio of ultimate displacement to yield displacement is used to express as the displacement ductility ratio of the shear walls. The greater the displacement ductility ratio, the better the ductility of the shear walls. As shown in Table 4, due to the existence of the Bauschinger effect, there are differences in load and displacement between positive and negative loading. Therefore, in this paper, the displacement ductility ratios in both directions of the specimens are calculated according to Equation (2), and the plastic rotation angle is determined by Equation (3) as an indicator to measure the ductility change in the shear walls. The calculation results are listed in Table 4. Equations (2) and (3) are as follows:

$$\mu = \Delta_{\mathrm{u}}/\Delta_{\mathrm{y}} \tag{2}$$

$$\theta_{\mathrm{p}} = (\Delta_{\mathrm{u}} - \Delta_{\mathrm{y}})/H \tag{3}$$

where μ is the displacement ductility ratio; θ_{p} is the plastic rotation angle; H is the calculated height of the specimens.

When comparing SW-3 with SW-4, it is found that with the increase in the height of the corroded area, that is, when the height of the corroded area increases from 15% to 25% of the total height, both the displacement ductility ratio and plastic rotation angle of the specimens gradually decrease, and in the positive loading direction, the displacement ductility ratio and plastic rotation angle are decreased by 46.5% and 52.9%, respectively, while in the negative loading direction, the displacement ductility ratio and plastic rotation angle are decreased by 17.1% and 29.9%, respectively. However, Zheng et al. [31] found that, in the overall corrosion test of squat RC shear walls under a salt spray environment, when the average mass loss of the steel bars was less than 12.32%, the displacement ductility ratio of the shear walls had been reduced to 71.0% of that of the uncorroded shear wall, indicating that compared with the overall corrosion, partial corrosion has a larger impact on the ductility of shear walls.

Compared with SW-2, the displacement ductility ratio and plastic rotation angle of SW-3 in the positive loading direction are decreased by 0.3% and 26.1%, respectively. The damage caused by positive loading affects negative loading, and in the negative loading direction, the displacement ductility ratio increases, but the plastic rotation angle still decreases. Compared with the uncorroded SW-1, the displacement ductility ratio and plastic rotation angle of SW-2 in the positive loading direction are increased by 33.0% and 31.7%, respectively, and in the negative loading direction, the displacement ductility ratio and plastic rotation angle are increased by 5.3% and 10.6%, respectively.

3.6. Shear Deformation Analysis

The calculation diagram of the shear deformation is shown in Figure 13, which is calculated according to Equations (4) and (5), and the calculated results are tabulated in Table 5.

$$\Delta_s = \frac{1}{2}\left[\sqrt{(l+\Delta_2)^2 - l^2} - \sqrt{(l+\Delta_1)^2 - l^2}\right] \tag{4}$$

$$\gamma = \frac{\Delta_s}{h} \tag{5}$$

where γ is the shear strain; l is the original length of displacement meter; Δ_1 and Δ_2 are length variations; h is the height of the wall.

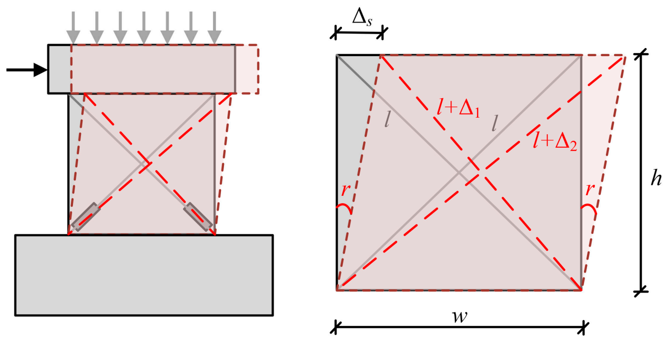

Figure 13. Diagram for the calculation of shear deformation.

Table 5. Shear strain and the ratio of shear deformation to horizontal displacement.

Loading Direction	Specimen Label	Cracking Point		Yield Point		Peak Point	
		γ	Δ_s/Δ_c(%)	γ	Δ_s/Δ_y(%)	γ	Δ_s/Δ_m(%)
Positive	SW-1	1.198	34.24	4.093	54.46	9.439	67.91
	SW-2	0.382	32.75	2.372	38.26	5.387	41.81
	SW-3	0.437	24.99	1.376	27.34	4.878	40.60
	SW-4	0.360	10.30	1.150	14.52	2.908	25.25
Negative	SW-1	1.302	37.19	3.477	44.30	7.724	56.25
	SW-2	0.690	29.56	3.665	45.91	7.753	51.52
	SW-3	0.242	10.37	0.957	17.73	5.102	43.48
	SW-4	0.252	10.80	0.923	17.81	4.249	36.31

Due to the serious damage to the specimen when it is loaded to the ultimate state, the data recorded by the displacement meter cannot be used. Therefore, only the shear strain and the ratio of shear deformation to horizontal displacement at the cracking, yield, and peak points of the specimens are analyzed.

It can be seen from Table 5 that with the increase in horizontal displacement, the ratio of shear deformation to horizontal displacement at the cracking, yield, and peak points of each specimen shows an increasing trend. The reason maybe that in the early stage of loading, with the increase in horizontal displacement, the stress of the steel bars in the wall increases continuously to resist horizontal load, and bending deformation is the main deformation; subsequently, the cracks gradually appear in concrete, the steel bars—especially the distributed steel bars in the wall—gradually yield, and the bearing capacity cannot be further increased, resulting in an increasing ratio of shear deformation to horizontal displacement.

In the positive loading direction, compared with the uncorroded SW-1, the shear strain and the ratio of shear deformation to horizontal displacement of SW-2 decrease, and the shear strains at the cracking, yield, and peak points are decreased by 68.1%, 42.0%, and 42.9%, respectively, while the ratios of shear deformations to horizontal displacements are decreased by 4.4%, 29.7%, and 38.4%, respectively. However, in the negative loading direction, the changes in the shear strain and the ratio of shear deformation to horizontal displacement are irregular.

When comparing SW-1, SW-3, and SW-4, when the height of the corroded area increases from 0 to 15% and 25% of the total height, in the positive loading direction, the shear strain at the cracking point is decreased by 63.5% and 69.9%, respectively, the shear strain at the yield point is decreased by 66.4% and 71.9%, respectively, and the shear strain at the peak point is decreased by 48.3% and 69.2%, respectively. Therefore, with the increase in the height of the corroded area, the shear strain of specimens in the positive loading direction generally shows a decreasing trend. Compared with SW-1, in the negative loading direction, the shear strain at the cracking point of SW-3 and SW-4 is decreased by 81.4% and

80.6%, respectively, is decreased by 72.5% and 73.5% at the yield point, respectively, and is decreased by 33.9% and 45.0% at the peak point, respectively. In other words, with the increase in the height of the corroded area, the shear strain in the negative loading direction approximately shows a decreasing trend. In the positive loading direction, compared with SW-1, the ratio of shear deformation to horizontal displacement of SW-3 and SW-4 is decreased by 27.0% and 69.9% at the cracking point, 49.8% and 73.3% at the yield point, and 40.2% and 62.8% at the peak point, respectively. In the negative loading direction, compared with SW-1, the ratio of shear deformation to the horizontal displacement of SW-3 and SW-4 at the cracking point is decreased by 72.1% and 71.0%, is decreased by 60.0% and 59.8% at the yield point, and is decreased by 22.7% and 35.4% at the peak point, respectively. Zheng et al. [46] confirmed that, with the increase in steel corrosion degree, the shear deformation and the ratio of shear deformation to horizontal displacement of specimens at the peak point decreased continuously, which is in agreement with the results obtained in this paper.

Compared with SW-2, the shear strain and the ratio of shear deformation to horizontal displacement of SW-3 decrease, and the shear strain is decreased by 42.0% and 9.4%, respectively, at the yield and peak points in the positive loading direction, and in the negative loading direction, the shear strain at the yield and peak points is decreased by 73.9% and 34.2%, respectively. In the positive loading direction, compared with SW-2, the ratio of shear deformation to horizontal displacement of SW-3 at the cracking point is reduced by 23.7%, point is reduced by 28.5% at the yield, and is reduced by 2.9% at the peak point, and in the negative loading direction, compared with SW-2, the ratio of shear deformation to horizontal displacement of SW-3 at the cracking point is decreased by 64.9%, is decreased by 61.4% at the yield point, and is decreased by 15.6% at the peak point.

The ratio of shear deformation to horizontal displacement decreases with the increase in the corroded area and corrosion height, while the corresponding proportion of bending deformation increases with the corrosion degree. This is mainly because the corrosion mainly occurs in the distributed steel bars with a thinner concrete cover, and the distributed steel bars mainly provide shear bearing capacity, and, relatively speaking, the hidden columns that provide flexural bearing capacity are less corroded due to the steel bars with a larger concrete cover thickness. Therefore, with the increase in corrosion degree, the shear bearing capacity decreases, and the ratio of shear deformation to horizontal displacement decreases.

3.7. Stiffness Degradation

From the hysteretic curve of each specimen, it can be seen that the stiffness of the specimens decreases with the increase in loading cycles and horizontal displacement. The equivalent stiffness at each point on the skeleton curve of the specimens is calculated according to Equation (6), and the variation in the positive and negative equivalent stiffness K_i of each specimen with the horizontal displacement is shown in Figure 14. Equation (6) is as follows:

$$K_i = \frac{|\pm P_i|}{|\pm \Delta_i|} \tag{6}$$

where $+P_i$ and $-P_i$ are the peak loads in the positive and negative directions during the loading of the *i*th level of horizontal displacement, respectively, kN; $+\Delta_i$ and $-\Delta_i$ are the peak displacements in the positive and negative directions during the loading of the *i*th level of horizontal displacement, respectively, mm.

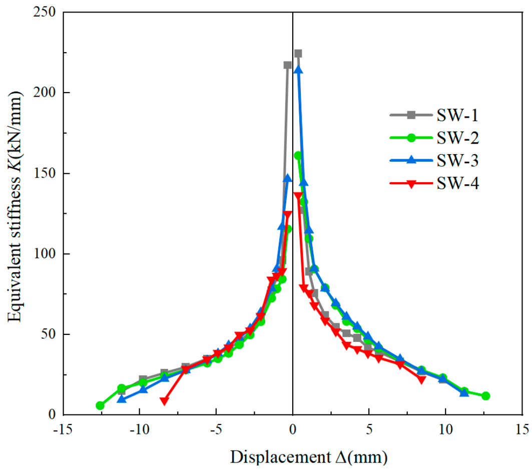

Figure 14. Degradation curves of equivalent stiffness.

Figure 14 shows that the degradation curves of the equivalent stiffness present an incomplete symmetry in the positive (push) and negative (pull) loading directions. The reason is that, due to the Bauschinger effect, the damage occurs first during positive loading, and the cumulative damage causes the stiffness of the shear walls to degrade faster under negative loading. The stiffness of specimens under different corrosion conditions is relatively large at the initial loading stage but gradually deteriorates with the increase in horizontal displacement. The initial stiffness is shown in Table 4. The specimens in the initial loading stage are in the elastic stage with relatively large stiffness, and in the range of small horizontal displacement, the stiffness rapidly drops to less than half of the initial stiffness, which indicates that cracks appear and develop continuously at this stage. Subsequently, the stiffness degradation rate gradually slows down; at this time, the existing cracks continue to expand and play a dominant role. With the increase in displacement, the steel bars inside the walls gradually yield and the concrete undergoes spalling, so the stiffness continues to decrease. When the damage of walls is more serious in the later stage of loading, the stiffness gradually tends to zero.

When comparing SW-1, SW-3, and SW-4, the trend of the stiffness degradation curves is basically the same. The initial stiffness of the uncorroded specimen is larger, and the initial stiffness gradually decreases with the increase in the height of the corroded area. According to the stiffness degradation trend shown in Figure 14, compared with other specimens, the stiffness of the SW-4 with a higher corroded area is degraded to zero at a lower horizontal displacement. When comparing SW-2 with SW-3, the stiffness degradation curves of the two are approximately coincident, indicating that the influence of unilateral corrosion or bilateral corrosion on the overall stiffness of the specimens is small. The overall trend of stiffness degradation of different specimens is consistent. When comparing SW-1 with SW-2, the initial stiffness of the uncorroded specimens is larger, while the stiffness degradation of the specimen with unilateral corrosion is relatively slow. This phenomenon can be attributed to two main factors. Firstly, SW-1 likely possesses initial manufacturing defects, causing a rapid degradation in specimen stiffness when subjected to a load. Secondly, after unilateral corrosion, the bond slip between steel bars and concrete is enhanced by the emergence of corrosion products, resulting in a slower degradation of stiffness in SW-2.

4. Conclusions

The seismic performance of partially corroded squat RC shear walls has been studied by the accelerated corrosion test and quasi-static test in this paper. The main conclusions are as follows:

(1) With the increase in the height of the corroded area, the horizontal displacement corresponding to the failure of the shear walls decreases. The horizontal displacement

corresponding to the failure of the bilateral corroded shear wall is less than that of the unilateral corroded shear wall. Compared with the uncorroded shear wall, the horizontal displacement corresponding to the failure of the unilateral corroded shear wall increases.

(2) Compared with the uncorroded shear wall, the hysteresis loop of the unilateral corroded shear wall is plump. With the increase in the height of the corroded area, the area of the hysteresis loop decreases obviously. The areas of the hysteresis loops of unilateral corroded and bilateral corroded shear walls are approximately equal.

(3) With the increase in the height of the corroded area, the peak and ultimate displacements of the shear wall are reduced. Compared with the unilateral corroded shear wall, the yield, peak, and ultimate displacements of the bilateral corroded shear wall are, respectively, reduced by 18.8%, 6.7%, and 19.2% in the positive loading direction and are, respectively, reduced by 32.4%, 22.3%, and 18.3% in the negative loading direction. Compared with the uncorroded shear wall, the yield and peak loads of the unilateral corroded shear wall show an increasing and a decreasing trend in the positive and negative loading directions, respectively.

(4) When the height of the corroded area increases from 15% to 25% of the total height, both the displacement ductility ratio and the plastic rotation angle decrease. Compared with the unilateral corroded shear wall, the displacement ductility ratio and plastic rotation angle of the bilateral corroded shear wall decrease by 0.3% and 26.1% in the positive loading direction, respectively. Compared with the uncorroded shear wall, both the displacement ductility ratio and plastic rotation angle of the unilateral corroded shear wall increase.

(5) Compared with the uncorroded shear wall, in the positive loading direction, the shear strain and the ratio of shear deformation to horizontal displacement of the unilateral corroded shear wall are reduced. With the increase in the height of the corroded area, the shear strain tends to decrease, and the ratio of shear deformation to horizontal displacement at the cracking, yield, and peak points decreases. Compared with the unilateral corroded shear wall, the shear strain and the ratio of shear deformation to the horizontal displacement of the bilateral corroded shear wall are also reduced.

(6) With the increase in the height of bilateral corroded area, the initial stiffness of the shear walls gradually decreases. Whether unilateral or bilateral corrosion occurs has little effect on the overall stiffness of the shear walls. Compared with the uncorroded shear wall, the stiffness degradation of the unilateral corroded shear wall is relatively slow.

Recommendations:

(1) This study is constrained by a limited number of test samples, which may influence the results to some extent. However, reasonable and largely different corrosion conditions have been used to carry out the test, which reduces the impact of the defect of small test samples. Therefore, the overarching trends observed in the study make the findings relatively reliable. To enhance future research on partially corroded RC shear walls and to establish more dependable and general rules, it is advisable to maximize the sample size. This paper exclusively examines squat RC shear walls, necessitating further verification to determine if similar patterns exist in other structural forms under local corrosion conditions.

(2) In coastal environments, the corrosion of shear walls is often influenced by factors, such as temperature, humidity, chloride ion concentration, etc. Therefore, the durability of these shear walls undergoes continuous changes. Due to the significant harm caused by local corrosion induced by chloride ions erosion to shear walls, this paper specifically investigates the effect of local corrosion on the seismic performance of squat RC shear walls. Future research directions may explore the influence of other coastal environmental factors, apart from chloride ions, on the seismic performance of squat RC shear walls.

(3) Considering the use of an idealized specimen model in this experiment, accelerated corrosion is employed as an approximation for natural corrosion, and the actual shear wall structure is simplified. The similarity between the simplified model and the actual component needs to be further verified. If the conclusions of this study are directly extrapolated to real-world engineering applications, their practical utility still requires further investigation. The findings of this paper not only contribute to the enrichment of the seismic performance database for corroded squat RC shear walls but also serve as a valuable reference for structural engineers. This paper also aids in evaluating the seismic performance of existing partially corroded buildings in chloride ion environments and formulates rational maintenance strategies. These strategies aim to extend the service life of shear walls and to ensure that they consistently exhibit excellent seismic performance throughout their service life.

Author Contributions: Conceptualization, J.W.; data curation, J.D.; formal analysis, Y.S.; investigation, Y.S. and J.D.; methodology, J.W.; supervision, J.W.; writing—original draft, Y.S.; writing—review and editing, J.W. and J.D. All authors have read and agreed to the published version of the manuscript.

Funding: This research received no external funding.

Data Availability Statement: The data presented in this study are available on request from the corresponding author. The data are not publicly available due to privacy.

Conflicts of Interest: The authors declare that there are no conflicts of interest.

References

1. Li, H.; Li, B. Experimental study on seismic restoring performance of reinforced concrete shear walls. *Build. Struct.* **2004**, *25*, 35–42.
2. Xu, L.; Xiao, S.; Li, Z. Experimental investigation on the seismic behavior of a new self-centering shear wall with additional friction. *J. Struct. Eng.* **2021**, *147*, 4021056. [CrossRef]
3. Zhou, Y.; Zheng, S.; Chen, L.; Long, L.; Dong, L.; Zheng, J. Experimental and analytical investigations into the seismic behavior and resistance of corroded reinforced concrete walls. *Eng. Struct.* **2021**, *238*, 112154. [CrossRef]
4. Gullu, M.F.; Orakcal, K. Nonlinear finite element modeling of reinforced concrete walls with varying aspect ratios. *J. Earthq. Eng.* **2021**, *25*, 2033–2064. [CrossRef]
5. Qian, J. *Structural Design of Tall Buildings*, 3rd ed.; China Architecture & Building Press: Beijing, China, 2018; p. 226.
6. Deng, M.; Fang, C.; Dai, J.; Liang, X. Experimental study on seismic behavior of high ductile fiber reinforced concrete low-rise shear walls. *Build. Struct.* **2017**, *47*, 57–63.
7. Rong, C.; Qu, Y.; Shah, A.A.; He, H. Seismic performance of energy dissipation low reinforced concrete shear wall with shear lead dampers. *Case Stud. Constr. Mater.* **2023**, *19*, e02276. [CrossRef]
8. Wang, J.; Yuan, Y.; Xu, Q.; Qin, H. Prediction of corrosion-induced longitudinal cracking time of concrete cover surface of reinforced concrete structures under load. *Materials* **2022**, *15*, 7395. [CrossRef] [PubMed]
9. Liu, X.; Jiang, H.; He, L. Experimental investigation on seismic performance of corroded reinforced concrete moment-resisting frames. *Eng. Struct.* **2017**, *153*, 639–652. [CrossRef]
10. Wang, J.; Ng, P.L.; Su, H.; Du, J. Influence of the coupled time and concrete stress effects on instantaneous chloride diffusion coefficient. *Constr. Build. Mater.* **2020**, *237*, 117645. [CrossRef]
11. Zhao, L.; Wang, J.; Gao, P.; Yuan, Y. Experimental study on the corrosion characteristics of steel bars in concrete considering the effects of multiple factors. *Case Stud. Constr. Mater.* **2023**, *20*, e02706. [CrossRef]
12. Guo, A.; Li, H.; Ba, X. Experimental investigation on the cyclic performance of reinforced concrete piers with chloride-induced corrosion in marine environment. *Eng. Struct.* **2015**, *105*, 1–11. [CrossRef]
13. Kashani, M.M.; Crewe, A.J.; Alexander, N.A. Nonlinear stress-strain behaviour of corrosion-damaged reinforcing bars including inelastic buckling. *Eng. Struct.* **2013**, *48*, 417–429. [CrossRef]
14. Van Nguyen, C.; Hieu Bui, Q.; Lambert, P. Experimental and numerical evaluation of the structural performance of corroded reinforced concrete beams under different corrosion schemes. *Structures* **2022**, *45*, 2318–2331. [CrossRef]
15. Feng, Q.; Visintin, P.; Oehlers, D.J. Deterioration of bond-slip due to corrosion of steel reinforcement in reinforced concrete. *Mag. Concr. Res.* **2016**, *68*, 768–781. [CrossRef]
16. Zhang, W.; Chen, H.; Gu, X. Bond behaviour between corroded steel bars and concrete under different strain rates. *Mag. Concr. Res.* **2016**, *68*, 364–378. [CrossRef]
17. Wang, J.; Ng, P.L.; Su, H.; Du, J. Meso-scale modelling of stress effect on chloride diffusion in concrete using three-phase composite sphere model. *Mater. Struct.* **2019**, *52*, 55. [CrossRef]

18. Yang, S.; Fang, C.; Yuan, Z.; Yi, Y. Effects of Reinforcement corrosion and repeated loads on performance of reinforced concrete beam. *Adv. Struct. Eng.* **2015**, *18*, 1257–1271. [CrossRef]
19. Vu, N.S.; Li, B. Seismic performance assessment of corroded reinforced concrete short columns. *J. Struct. Eng.* **2018**, *144*, 4018018. [CrossRef]
20. Oyamoto, T.; Nimura, A.; Okayasu, T.; Sawada, S.; Umeki, Y.; Wada, H.; Miyazaki, T. Experimental and analytical study of structural performance of RC shear walls with corroded reinforcement. *J. Adv. Concr. Technol.* **2017**, *15*, 662–683. [CrossRef]
21. Zheng, Y.; Zheng, S.; Yang, L.; Dong, L.; Ruan, S.; Ming, M. Experimental study on the seismic behavior of corroded reinforced concrete walls in an artificial climate corrosion environment. *Eng. Struct.* **2022**, *252*, 113469. [CrossRef]
22. Li, M.; Shen, D.; Yang, Q.; Cao, X.; Huang, C.; Cui, Z.; Qi, Y. Effect of reinforcement corrosion on the seismic performance of reinforced concrete shear walls. *Constr. Build. Mater.* **2023**, *377*, 130977. [CrossRef]
23. Yang, L.; Zheng, S.; Zheng, Y.; Dong, L.; Wu, H. Experimental investigation and numerical modeling of the seismic performance of corroded T-shaped reinforced concrete shear walls. *Eng. Struct.* **2023**, *283*, 115930. [CrossRef]
24. Su, R.K.L.; Wong, S.M. Seismic behaviour of slender reinforced concrete shear walls under high axial load ratio. *Eng. Struct.* **2007**, *29*, 1957–1965. [CrossRef]
25. Greifenhagen, C.; Lestuzzi, P. Static cyclic tests on lightly reinforced concrete shear walls. *Eng. Struct.* **2005**, *27*, 1703–1712. [CrossRef]
26. Dong, Q.; Xu, L.; Zhang, Y.; Xie, X. Cyclic response and parametric study of a self-centering coupled shear wall system with disc spring devices. *Soil Dyn. Earthq. Eng.* **2023**, *174*, 108214. [CrossRef]
27. Xu, G.; Zheng, L.; Zhou, W.; Zhai, C.; Wang, D. Quasi-static tests of squat reinforced concrete shear walls with openings. *Eng. Struct.* **2023**, *293*, 116666. [CrossRef]
28. Cheng, X.; Lu, C.; Ji, X.; Li, Y.; Song, Y. Seismic behavior of reinforced concrete slender walls subjected to variable axial loads. *Soil Dyn. Earthq. Eng.* **2023**, *175*, 108253. [CrossRef]
29. Yang, J.; Li, L.; Wang, X.; Hu, S. Experimental study on the seismic performance of concrete shear walls partially replaced by MRPC. *Case Stud. Constr. Mater.* **2024**, *20*, e02695. [CrossRef]
30. *GB 50010*; Code for Design of Concrete Structure. China Architecture & Building Press: Beijing, China, 2015.
31. Zhang, W.; Song, X.; Gu, X.; Li, S. Tensile and fatigue behavior of corroded rebars. *Constr. Build. Mater.* **2012**, *34*, 409–417. [CrossRef]
32. Wang, X.; Zhang, W.; Cui, W.; Wittmann, H.F. Bond strength of corroded steel bars in reinforced concrete structural elements strengthened with CFRP sheets. *Cem. Concr. Compos.* **2011**, *33*, 513–519. [CrossRef]
33. Azad, A.K.; Ahmad, S.; Azher, S.A. Residual strength of corrosion-damaged reinforced concrete beams. *ACI Struct. J.* **2007**, *104*, 40–47.
34. Wang, X.; Gu, X.; Zhang, W. Flexural stiffness of corroded reinforced concrete beams strengthened with carbon fiber composite sheets. *J. Build. Struct.* **2009**, *30*, 169–176.
35. Zhao, Y.; Wang, Y.; Dong, J. Prediction of corrosion-induced concrete cracking under external loading and stirrup constraint. *Constr. Build. Mater.* **2021**, *266*, 121053. [CrossRef]
36. Yang, O.; Zhang, B.; Yan, G.; Chen, J. Bond performance between slightly corroded steel bar and concrete after exposure to high temperature. *J. Struct. Eng.* **2018**, *144*, 04018209. [CrossRef]
37. Coronelli, D.; Hanjari, K.Z.; Lundgren, K. Severely corroded RC with cover cracking. *J. Struct. Eng.* **2013**, *139*, 221–232. [CrossRef]
38. Su, T. Experimental Study on Seismic Behavior and Numerical Simulation Analysis of Low-Rise Concrete Shear Wall. Master's Thesis, Harbin Institute of Technology, Harbin, China, 2021.
39. Zheng, S.; Zhou, Y.; Li, Q.; Dong, L.; He, J. Experimental study on aseismic behavior of squat RC shear walls due to chloride ion erosion. *Eng. Mech.* **2019**, *36*, 69–78.
40. *JGJ/T101*; Specification for Seismic Test of Buildings. China Architecture & Building Press: Beijing, China, 2015.
41. *GB/T 50082*; Standard for Test Methods of Long-Term Performance and Durability of Ordinary Concrete. China Architecture & Building Press: Beijing, China, 2009.
42. Xiao, Y.; Zeng, L.; Cui, Z. Experimental and analytical performance evaluation of steel beam to concrete-encased composite column with unsymmetrical steel section joints. *Steel Compos. Struct.* **2017**, *23*, 17–29. [CrossRef]
43. Ma, Y.; Che, Y.; Gong, J. Behavior of corrosion damaged circular reinforced concrete columns under cyclic loading. *Constr. Build. Mater.* **2012**, *29*, 548–556. [CrossRef]
44. Woods, J.E.; Lau, D.T.; Cruz-Noguez, C.A. In-plane seismic strengthening of nonductile reinforced concrete shear walls using externally bonded CFRP sheets. *J. Compos. Constr.* **2017**, *20*, 04016052. [CrossRef]
45. Jafari, A.; Beheshti, M.; Shahmansouri, A.A.; Bengar, H.A. Plastic hinge length for coupled and hybrid-coupled shear walls. *Steel Compos. Struct.* **2023**, *48*, 367–383.
46. Zheng, Y.; Zheng, S.; Dong, L.; He, J.; Ming, M. Experimental study on the seismic behavior of RC shear walls in a simulated acid environment. *Eng. Mech.* **2020**, *37*, 190–198.